ACS APPLIED MATERIALS & INTERFACES

www.acsami.org Research Article

Fluorescence Turn-on Detection of Perfluorooctanoic Acid (PFOA) by Perylene Diimide-Based Metal−Organic Framework

Rana Dalapati, Matthew Hunter, Mostakim SK, Xiaomei Yang, and Ling Zang*

Cite This: *ACS Appl. Mater. Interfaces* 2024, 16, 32344−32356 **Read Online**

ACCESS | Metrics & More | Article Recommendations | Supporting Information

ABSTRACT: A novel, water-stable, perylene diimide (PDI) based metal−organic framework (MOF), namely, **U-1**, has been synthesized for selective and sensitive detection of perfluorooctanoic acid (PFOA) in mixed aqueous solutions. The MOF shows highly selective fluorescence turn-on detection via the formation of a PFOA-MOF complex. This PFOA-MOF complex formation was confirmed by various spectroscopic techniques. The detection limit of the MOF for PFOA was found to be 1.68 μM in an aqueous suspension. Upon coating onto cellulose paper, the MOF demonstrated a significantly lower detection limit, down to 3.1 nM, which is mainly due to the concentrative effect of solid phase extraction (SPE). This detection limit is lower than the fluorescence sensors based on MOFs previously reported for PFAS detection. The MOF sensor is regenerable and capable of detecting PFOA in drinking and tap water samples. The PDI-MOF-based sensor reported herein represents a novel approach, relying on fluorescence turn-on response, that has not yet been thoroughly investigated for detecting per- and polyfluoroalkyl substances (PFAS) until now.

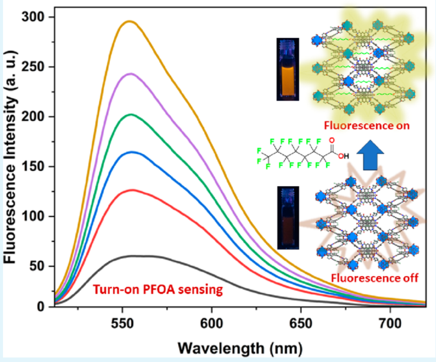

KEYWORDS: *Metal−organic framework (MOF), Perfluorooctanoic acid (PFOA), Fluorescent sensor, Fluorescence turn-on, Perylene diimide (PDI)*

INTRODUCTION

Per- and polyfluoroalkyl substances (PFAS) are a large group of laboratory-made fluorinated hydrocarbons (FHC) used to manufacture hydrophobic coatings and products.[1] PFAS are present in a variety of products, including nonstick cooking surfaces, furniture, aqueous film forming foam (AFFF) for fire extinguishing, adhesives, food packaging, clothing, and the insulation of electrical wire.[2−4] The most used PFAS are perfluorooctanoic acid (PFOA) and perfluorooctanesulfonic acid (PFOS).[5,6] PFOA has found extensive applications in the manufacturing of various industrial and consumer goods, including notable products such as Teflon and Gore-Tex. Due to robust carbon−fluorine bonds, PFOA does not readily degrade in the environment, resulting in its widespread accumulation and bioaccumulation. Through industrial production and widespread utilization, PFOA can easily permeate soil, sludge, groundwater, and air. Early epidemiological studies found "probable links" between PFOA exposure and high cholesterol, pregnancy-induced hypertension, thyroid illness, kidney and testicular cancer.[7] The research has also disclosed that PFAS may affect the growth and learning behavior of newborns, reduce vaccine-induced immunity in children, affect the body's natural hormone production and immune system, and increase the risk of some cancers. According to a recent report, several lakes are highly contaminated near the U.S. military bases where PFAS-based foam is used for fire quenching.[8,9] Because of their high stability and persistence in the environment, PFAS compounds have a predisposition to bioaccumulate. The uptake of PFAS into plants and fish can occur within contaminated areas and can subsequently move into the food chain, potentially affecting wildlife and humans who consume these organisms. In this way, toxic PFAS compounds are bioaccumulated and subsequently biomagnified up the food chain.[10−12] PFAS are already found in the blood of people and animals in various countries all over the world, which is alarming considering their adverse health effects.[13,14] Therefore, the detection of toxic PFAS in contaminated water is becoming increasingly essential.

Currently, the standard detection techniques for PFAS primarily rely on liquid chromatography coupled with mass spectrometry.[15,16] The EPA approved official analytical techniques (e.g., Method 533, 537 and 1633) to study different PFAS concentrations in water samples including drinking water. These methods rely on solid-phase extraction (SPE)-enabled liquid chromatography-tandem mass spectrometry (LC-MS/MS).[17−19] Although the LC-MS method is

Received: February 29, 2024
Revised: May 4, 2024
Accepted: May 6, 2024
Published: May 8, 2024

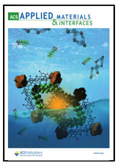

https://doi.org/10.1021/acsami.4c03389

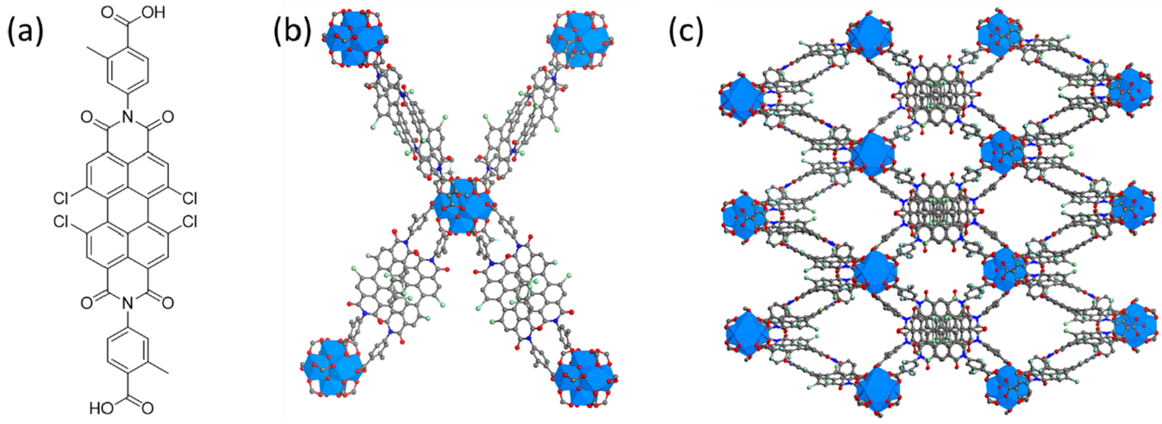

Figure 1. (a) Chemical structure of the PDI based ligand, H_2**L**, used in this study; (b) Connection mode of Zr-cluster and molecular arrangement of the ligand, and (c) a-Axis crystal structure of **U-1**.

accurate, it requires highly trained laboratory personnel, complex instrumentation, difficult sample preparation, and tedious data collection. In recent years, numerous efforts have attempted to design new PFAS detection platforms that are not mass spectrometry dependent, are cost-effective, have fast response times, and are easy to use for onsite PFAS detection.[20−23] Among all the new detection techniques developed, optical sensors based on molecular or nanostructured materials have intrinsic advantages like fast response time, easy operation, cost effectiveness, naked eye identification, and the potential to build hand-held sensor devices for onsite detection. Particularly, fluorescent sensors have attracted increasing interest due to high sensitivity toward target analytes. There have been several fluorescent sensors recently developed to detect PFAS.[24−32] Unfortunately, most of these reported sensors lack sufficient selectivity, making it difficult to distinguish between different PFASs. Considering real-world applications where mixtures of PFASs may exist, it is essential to develop a new fluorescent sensor that can discriminatively detect different PFASs. Selective detection of PFAS is also critical for assessing the transport of different types of PFAS in the environment and monitoring the effectiveness of on-site abatement processes.

Fluorescent metal−organic frameworks (MOFs) have evolved as a new-generation functional material because of their ultrahigh porosity, large surface area, structural diversity and tunability.[33,34] Owing to these unique properties, a large number of MOF-based sensors have been developed in recent years for a broad range of applications in the fields of turn-on and turn-off fluorescence sensing.[35−37] These applications include detection of volatile organic compounds,[38] explosives,[39,40] biomolecules,[41,42] carcinogens,[43] heavy metals,[44,45] anticounterfeit materials,[46] and many more.[47−49] Very recently, three known zirconium porphyrinic MOFs (PCNs, i.e., PCN-222, PCN-223, and PCN-224) have been explored for PFAS detection using sensor arrays,[50] which all rely on fluorescence "turn-off" response upon interacting with PFASs. However, the "turn-off" approach may result in false positives in detection due to the unspecific fluorescence quenching caused by other contaminants in the sample, considering their application in real sample analysis. In contrast, using fluorescence "turn-on" probes that switch their fluorescence from "off" (or low intensity) to "on" (or high intensity) would help enhance the signal-to-noise ratio by reducing the background signal, which should result in improved detection sensitivity. Therefore, we believe that developing new fluorescence "turn-on" sensors based on MOF materials remains crucial for the detection and discrimination of PFAS present in environmental samples.

Herein we report the design and synthesis of a non-fluorinated, water-stable MOF with hydrophobic 3,4,9,10-Perylenetetracarboxylic diimide (PDI) as the ligand (Figure 1), namely, **U-1** (U= University of Utah), for discriminative fluorescence turn-on detection of PFOA over PFOS and other common alkyl acids. Considering PFOS and PFOA are the two most prevalent forms of PFAS contaminating the environment, this work focused on the detection of these two compounds with sensitivity and selectivity as primary foci. Molecules and materials of PDIs show high thermal stability and photostability under ambient conditions, which makes them a suitable platform for optoelectronic device fabrication for chemical sensing.[51,52] Numerous PDI molecules yield well-defined supramolecular nanostructures driven by self-assembly.[53,54] The PDI molecules, with coordinating carboxyl or pyridyl functional groups, undergo a coordination-driven self-assembly with metal ions.[55−57] Coordination driven self-assembly generally forms one-dimensional or two-dimensional morphologies, which inhibits the porosity of coordination compounds. Very few PDI based, porous MOFs have been reported as of yet due to these drawbacks.[49,58−60]

The newly reported PDI-based MOF, **U-1**, is comprised of a methyl functionalized 1,2,6,7-tetrachloroperylene-3,4,9,10-tetracarboxylic acid diimide ligand (H_2**L**) and $Zr_6(\mu_3\text{-}O)_4(\mu_3\text{-}OH)_4$ clusters. The tetrachloro-substitution increases the solubility of the PDI ligand during MOF synthesis, whereas the judicious incorporation of methyl groups increases the hydrophobicity around the Zr_6 SBUs in the MOF. This minimizes the interaction with water molecules, which in turn helps to enhance the stability of the MOF in water. We chose zirconium metal ion for the MOF synthesis because of its binding affinity toward PFAS molecules, like PFOA, that contain carboxylic groups.[61,62] The PDI-based MOF showed a rapid fluorescence turn-on response toward PFOA in aqueous solutions. Although similar in structure, PFOS did not demonstrate a significant turn-on response compared to PFOA. This reusable MOF sensor can detect the presence of PFOA in real water samples, including tap water and drinking water. The rapid turn-on sensing via a MOF-PFOA complex formation mechanism may soon lead to this material being an efficient dual sensor and absorber for PFAS. To the best of our knowledge, this is the first example of a MOF-based

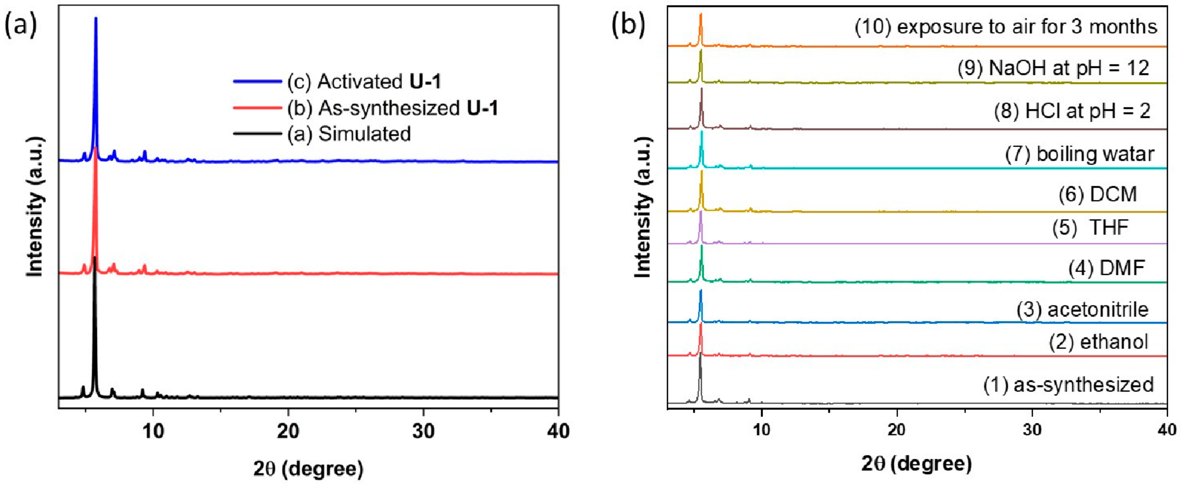

Figure 2. (a) PXRD patterns measured with the as-synthesized and activated **U-1** MOF in comparison to the simulated patterns. (b) Stability tests of the **U-1** MOF sample treated under various conditions as characterized by PXRD measurement.

fluorescence turn-on sensor for the rapid, discriminative detection of PFOA in water samples.

EXPERIMENTAL SECTION

Materials and Physical Measurements. All reagent grade starting materials and PFASs were used as received from commercial suppliers. Milli-Q water was used for the preparation of the analyte stock solutions. Fourier transform infrared (FT-IR) spectra were collected in the region of 440−4000 cm^{-1} with a Nicolet iS50 FT-IR spectrometer. Thermogravimetric analyses (TGA) were carried out with a TA Instruments Discovery SDT 650 thermogravimetric analyzer in the temperature range of 30−700 °C in an air atmosphere. Ambient-temperature powder X-ray diffraction (PXRD) patterns were measured on a Bruker D2 Phaser X-ray diffractometer operated at 30 kV and 10 mA by using Cu Kα (λ = 1.5406 Å) radiation. The nitrogen sorption isotherms up to 1 bar were recorded using a Micromeritics 3Flex gas sorption analyzer at −196 °C. Before the sorption measurement, the compound was degassed at 80 °C for 24 h under a dynamic vacuum. Steady-state fluorescence studies were carried out using an Agilent Cary Eclipse fluorescence spectrophotometer. Fluorescence images were taken with a Leica DMi8 fluorescent microscope. NMR data were recorded on a Varian Mercury 400 MHz spectrometer. X-ray photoelectron spectroscopy (XPS) measurements were performed using a Kratos Axis Ultra DLD X-ray spectrometer. Thermo Scientific Advantage Data System software was used for data analysis, with the C 1s reference peak at 284.8 eV. A Bruker maXis II ETD Q-TOF LC/MS instrument was used to obtain high-resolution ESI MS data. Scanning electron microscopy (SEM) images were obtained on an FEI Nova NanoSEM scanning electron microscope.

Synthesis of H_2L ligand. 1,6,7,8-tetrachloroperylene-3,4,9,10-tetracarboxylic acid dianhydride (1.00 g, 1.89 mmol), 4-amino-2-methylbenzoic acid (2.85 g, 18.9 mmol), and propionic acid (25 mL) were stirred at 150 °C for 20 h. The resulting mixture was then cooled to room temperature, followed by the addition of water to the mixture. The resulting precipitate was filtered, washed with a mixture of methanol and water (1:1), and dried under a vacuum to obtain an orange solid. This solid was then subjected to recrystallization twice with DMF, resulting in the final desired product (orange powder). Yield: 1.06 g (70%)

^{1}H NMR (400 MHz, DMSO) δ: 8.61 (s, 4H), 7.98 (d, 2H), 7.35 (m, 4H), 2.59 (s, 6H). ESI-MS (*m*/*z*): [M-H+] Calcd 793.98, found 792.97. The NMR and mass spectra of the H_2**L** ligand are shown in Figures S1 and S2.

Synthesis of U-1. A mixture of $ZrCl_4$ (29 mg, 0.125 mmol), H_2**L** ligand (50 mg, 0.0625 mmol) and trifluoroacetic acid were dissolved in 15 mL of *N*,*N*-dimethylformamide (DMF) by sonication for 10 min. The resulting dark red solution was transferred into a Teflon liner and heated at 100 °C for 24 h. After being cooled to room temperature, the red powder was collected by filtration and washed with large volumes of DMF and acetone. After filtration, the MOF sample was dried in an oven.

Activation of the As-Synthesized Material. The **U-1** MOF (30 mg) was stirred for 24 h in 50 mL of chloroform to replace the high boiling point solvent, DMF. The powder sample was then separated and heated in a vacuum oven at 80 °C for 24 h to completely remove chloroform. This desolvated **U-1** MOF sample was used for further analysis.

Pawley Refinement. The powder X-ray diffraction (PXRD) pattern of **U-1** was measured in a reflection geometry using CuKα1 radiation and indexed with the help of STOE WinXPow software[63] (Found: *I*-centered cell, a = b = 18.885(13) Å and c = 83.056(22) Å with a space group, $I\ 4_1/a$). In **U-1**, the model of the methyl functionalized PTCDI ligand molecule was similar to the ligand molecule used previously by Lü et al. to make Zr-PDI MOF.[58] This structural simulation and refinement are necessary since the ligand molecule in **U-1** has a methyl-functional group, and trifluoroacetic acid (TFA) was used as a modulator. The simulated structure was obtained by imposing the structure of Zr-PDI, converting the ligand molecule, and subsequently optimized by force-field calculation using the universal force field as implemented in the Materials Studio software.[64] An attempted full Pawley refinement of this model was not possible, which we attribute to the length of the ligand molecule, the large unit cell, and the low number of reflections above 20°. Some relevant cell parameters for the modeling are summarized in Table S1 and the final plot is shown in Figure S3. The simulated PXRD data correlate suitably with the experimental data (Figure 2), although the peak intensities deviate from the data stated above.

Sensing Experiments for PFAS. The suspension of activated **U-1** MOF was prepared by dispersing 6 mg of the MOF powder in 3 mL of DMF. The mixtures were sonicated for 30 min to create homogeneity throughout the dispersion before fluorescence measurements were taken. 0.2 mL of the as-prepared stock solution were mixed with 2.8 mL of water/DMF (60/40 v/v) in a quartz cuvette (final MOF concentration: 0.13 mg/mL). The emission spectra of the **U-1** MOF suspension were obtained at an excitation wavelength (λ_{ex}) of 490 nm. The analytes and interferents used for the sensor testing experiments were PFOA, PFOS, octanoic acid, lauric acid, trifluoroacetic acid (TFA), and cetyltrimethylammonium bromide (CTAB), for which 10 mM stock solutions were prepared in water. Selected PFAS and other interferents were added gradually into the **U-1** suspension, and the mixture was thoroughly mixed before recording the fluorescence spectra. The spectra were recorded three times for each sample, and the averaged data were plotted to ensure accuracy and reliability.

Filter Paper Based PFOA Detection. The **U-1** MOF was coated on Whatman filter paper (~1 × 1 cm) by immersing the paper in a MOF suspension made in ethanol, followed by oven drying. The process was repeated three times to increase MOF loading on the paper strip. The MOF loading amount was ~5 mg/cm^2 (measured by taking weight before and after loading). Fifteen μL of various low concentration (10−50 nM) solutions of PFOA were added to paper strips (~1 cm × 1 cm) and solvents were subsequently dried. The process was repeated five times (total volume added 75 μL) to ensure adequate accumulation of PFOA. Finally, 10 μL DMF was added to the PFOA accumulated paper and emission intensity was measured.

Regeneration of MOF. After each consecutive sensing cycle, the MOF suspension was carefully transferred to a centrifuge tube. The solution was then subjected to centrifugation for 10 min at 4000 rpm. The supernatant solution was decanted, and 10 mL of a 30/70 v/v mixture of 0.1 M HCl and methanol was added. This mixture was sonicated for 30 min before being centrifuged at 4000 rpm for 10 min to collect the MOF particles. This process was repeated three times. The MOF was then washed twice with deionized water followed by acetone and collected via centrifugation. The regenerated MOF was dried in a vacuum oven at 60 °C before the next sensing experiment.

Quantum Yield Calculation. The fluorescence quantum yield of the **U-1** MOF, before and after PFOA sensing, was evaluated by the Parker-Rees method using Rhodamine 6G as a standard fluorophore. The Parker-Rees equation can be written as follows:[65,66]

$$\Phi_u = (A_s F_u n_u^2 / A_u F_s n_s^2)\Phi_s \qquad (1)$$

Where Φ_s represents the quantum yield of the reference compound (Rhodamine 6G, with a value of 0.95) and Φ_u denotes the quantum yield of the MOF sample. A_s and A_u stand for the absorbances of Rhodamine 6G and the MOF sample at the excitation wavelength (490 nm), respectively. To mitigate the reabsorption of fluorescence light passing through the samples, the absorbance maxima were maintained below 0.1. F_s and F_u denote the integrated fluorescence intensity areas of Rhodamine 6G and the MOF sample when excited at the same wavelength, respectively. The refractive indices of the solvents for the MOF sample suspension and Rhodamine 6G are denoted by n_u and n_s respectively.

RESULTS AND DISCUSSION

Synthesis and Activation of U-1 MOF. Initially, we followed the synthesis procedure recently reported by Lü et al. on the only other perylene diimide based MOF (Zr-PDI) with a similar PDI ligand by using acetic acid as a modulator.[58] Unfortunately, we did not obtain any crystalline MOF material with our new PDI ligand (H_2**L**). As a result, we explored alternative synthesis conditions using different zirconium salts ($ZrCl_4$ and $ZrOCl_2{\cdot}8H_2O$) and dimethylformamide (DMF) as a solvent. We varied the temperature and time of the reaction, as well as tested different modulators: benzoic acid, acetic acid, formic acid, proline, and trifluoroacetic acid. This was done to increase the crystallinity of the MOFs (Table S2). Optimized synthesis conditions were achieved by using $ZrCl_4$ as the metal salt, trifluoroacetic acid as the modulator, and DMF as the solvent. Crystalline powder of **U-1** MOF was obtained by heating the reaction mixture for 24 h at 100 °C. The significant difference in synthesis protocol between **U-1** and the previous Zr-PDI MOF is the methyl modification at the benzoic group of the PDI ligand, which changes the local hydrophobicity around the metal cluster.

Structure Description. **U-1** MOF was produced by the solvothermal reaction between H_2**L** (Figure 1a) and $ZrCl_4$ in DMF at 100 °C with TFA as a modulator. The PXRD patterns of **U-1** were in tetragonal crystal system with the space group *I 41/a* with a = b = 19.2570(6) Å and c = 83.1554(7) Å. The Pawley refinement data indicates that **U-1** is isostructural with the Zr-PDI MOF recently reported by Lü et al.,[58] for which a similar tetrachloro-substituted PDI ligand was used, but without the methyl modification at the benzoic group. The six vertices of the $Zr_6(\mu_3\text{-O})_4(\mu_3\text{−OH})_4$ octahedral cluster are occupied by Zr(IV) centers and the eight triangular faces are alternatively capped by four μ_3−OH and four μ_3-O groups. The $[Zr_6(\mu_3\text{-O})_4(\mu_3\text{−OH})_4]^{12+}$ SBU is coordinated by 12 carboxylate units, 8 H_2**L** ligands, and 4 TFA molecules. The asymmetric unit of **U-1** contains two crystallographically independent Zr atoms, one L^{2-} ligand molecule, one TFA molecule and two μ_3-O atoms (Figure S4). Due to the electrostatic repulsion and steric hindrance arising from the tetrachloro- and methyl- substitutions, the central conjugated ring of H_2**L** ligand is highly twisted with a dihedral angle ∠(C−C−C−C) of 36.9° (Figure S5). This twisted structure of the H_2**L** ligand in the crystalline **U-1** MOF highlights the axial chirality of the PDI-based ligand. As depicted in Figure 1b and c, the $Zr_6(\mu_3\text{-O})_4(\mu_3\text{−OH})_4$ SBUs are connected to each other via the L^{2-} ligands, which form a 3D polymeric structure due to chirality differences. The results of Pawley refinement confirmed that the simulated and experimental PXRD data are identical to each other for **U-1** (Figure 2a).

Characterization of U-1. The phase purity of **U-1** was confirmed by PXRD measurements. The as-synthesized MOF material showed a good resemblance to the simulated PXRD pattern (Figure 2a). The PXRD pattern of activated **U-1** also well-matched with the simulated PXRD pattern. This suggests that the guest-free form of **U-1** has the same structural framework as that of the parent sample, implying the mechanical robustness of the framework during the activation process. The high intensity peaks in ATR-IR spectra around 1680 and 1383 cm^{-1} for **U-1** arise from the asymmetric and symmetric − COO− stretching vibrations, respectively, caused by the metal coordinated $\mathbf{L}^{2-}$ ligands (Figure S6). The peak near 1201 cm^{-1}, corresponding to C−F stretching, confirms the presence of a TFA molecule in the framework. The SEM images (Figure S7) reveal a uniform distribution of micrometer-sized MOF particles with minimal presence of amorphous materials, which provide additional confirmation of the material's phase purity.

MOFs constructed with large ligand molecules tend to undergo pore collapse upon solvent removal. Strong mechanical robustness and permanent porosity are remarkable properties for current MOFs constructed with PDI ligands (length >24 Å). N_2 sorption experiments were conducted to check the permanent porosity of the activated **U-1** MOF. The N_2 sorption isotherms of **U-1** agree with IUPAC classifications, following type I behavior (Figure S8). From the N_2 adsorption isotherm, the specific BET surface area of **U-1** was calculated to be 1263 m^2 g^{-1}. This again indicates that the **U-1** MOF can retain its porosity during the activation process.

To verify the chemical stability of **U-1** MOF, the powder material was immersed in different kinds of liquids (i.e., ethanol, acetonitrile, THF, DMF etc.) overnight. The MOF material was then recovered by centrifugation, and the PXRD patterns were recorded. The PXRD patterns of the solvent treated MOFs remained almost unchanged compared to the untreated sample (Figure 2b). These results suggest that the framework of **U-1** was unaffected when it was dispersed in various liquids. For PFAS detection applications, **U-1** must survive different pH media in industrial wastewater or environmental water. To confirm the framework stability of **U-1** in varying pH environments, the MOF powder was treated with HCl (pH = 2) and NaOH (pH = 10) solutions for 12 h. The PXRD patterns were then acquired. As depicted in Figure 2b, the PXRD patterns remain almost unchanged upon treatment in acid or base, further affirming strong chemical stability, which is conducive to sensor applications in a broad range of water samples. In addition to chemical stability, **U-1** also shows thermal stability up to 400 °C, as confirmed by thermogravimetric analyses (Figure S9). Thermal and chemical stabilities of **U-1** prove the relevance of the material for use in real-field chemical detection.

Photophysical Behavior. PDIs have received considerable attention as fluorophores due to their high photo and thermal stability in ambient conditions.[52,67−69] Based on the high structural tunability at the bay and imide positions, numerous molecules of PDI, and the assembled materials, have been developed as chemical sensors.[70−72] The PDI based fluorophore shows interesting emissive behavior in a fully dissolved state in solution. A strong tendency toward intermolecular $\pi-\pi$ stacking of PDI molecules leads to aggregation-caused quenching (ACQ), which decreases the emission in an aggregated or solid state. Such an ACQ phenomenon restricts the application of PDIs as a solid-state sensor material. Prevention of close $\pi-\pi$ stacking in solid state PDI is challenging. In MOFs, the ligand molecules can self-assemble via metal coordination in a well-defined manner in the crystal system. This is unique and not applicable to other types of self-assembly processes. The formation of a PDI ligand-based MOF could be beneficial to mitigate the ACQ effect on PDI fluorophores.

To verify this hypothesis, we first performed fluorescence microscopy measurements on the free ligand H_2**L** and **U-1** MOF deposited on a glass substrate (Figure S10a and b). **U-1** shows much stronger red emission compared to that of the free ligand under the same imaging condition. The observation is consistent with the fluorescence spectral measurement performed on the same samples (Figure S10c), for which the **U-1** MOF exhibits broad emission bandwidth maximum at 580 nm, while the aggregate of H_2**L** ligand shows much weaker emission with maximum wavelength shifted to ca. 605 nm. Red shift of emission band is characteristic of aggregation of PDI molecules.[52] The blue shift of emission maximum and increase in intensity observed for the **U-1** MOF is caused by the coordination of the PDI ligand to Zr(IV), which in turn weakens the $\pi-\pi$ stacking of PDI backbones and subsequently the ACQ effect. The presence of close shell d^0 electronic configuration of the Zr^{4+} metal ion also excludes any possibility for paramagnetic fluorescence quenching of the ligand molecules.[73] The UV−vis spectrum of **U-1** MOF shows two strong absorption bands near 543 and 496 nm, with a broad shoulder peak around 456 nm (Figure S11). This characteristic absorbance of **U-1** MOF could be assigned to the 0−0, 0−1, and 0−2 transition energies of the PDI molecule.[74] When compared to the molecularly dispersed state of H_2**L** ligand in solution phase with emission maximized at 552 nm (Figure S12), the fluorescence spectrum measured for the **U-1** MOF demonstrates an ~4 nm red shift. This implies a conformational change of the p-conjugation structure of PDI backbone, particularly the dihedral twisting angle around the four chloro-moieties. Additionally, when compared to the solid state and dispersed state emission of **U-1** in a binary water/DMF mixture, a significant blue shift was observed in the dispersed state (Figure S13). This can be attributed to the structurally relaxed state achieved through polar solvation processes in the high dielectric environment, as opposed to the solid state.[75] The interesting fluorescence behavior of the current MOF in both solid and dispersed states motivated us to investigate the impact of solvents on the MOF's emission. The fluorescence emission intensity of the MOF is notably reduced in water, the most polar solvent among those tested, as shown in Figure S14. On the contrary, solvents with lower polarity, such as methanol and tetrahydrofuran, exhibit higher fluorescence levels. This trend can be attributed to the pronounced dipole−dipole interactions between the twisted perylene core of the MOF and the solvent molecules, which is particularly evident in highly polar solvents. Consequently, solvents with elevated polarity effectively inhibit the radiative relaxation of the perylene core through strong interactions, leading to a decrease in the MOF's fluorescence. The MOF demonstrates its lowest fluorescence intensity in water, owing to its highest polarity among the selected solvents. The photostability of a potential sensor material remains a critical factor considered for real-world applications. Particularly, some PDI based materials may not be photostable under continuous irradiation.[76,77] The MOF suspension was continuously irradiated with UV light (λ = 365 nm, 6 W, provided by UVGL-58 hand-held UV Lamp) and emission maxima were monitored in time intervals. As depicted in Figure S15, almost no change in emission intensity was observed for **U-1** MOF even after 30 min of UV light irradiation. This confirms the photostability of the current, developed MOF. These results enabled us to develop the **U-1** MOF as a fluorescence turn-on sensor for chemicals like PFOA (*vide infra*) that may compete for binding with the same metal center, resulting in turning on the fluorescence emission of PDIs.

Detection of PFOA. As mentioned above, the unique photophysical property and porous nature of **U-1** MOF encouraged us to check its response toward PFOA. The Zr-PDI MOF, recently reported, does not possess the methyl groups at the phenyl moiety.[58] These prefunctionalized hydrophobic groups are especially critical for enhancing the binding and detection of hydrophobic target analytes, such as PFAS compounds, leveraging the strong hydrophobic interactions. The use of a methylated ligand also helps maintain hydrophobic pore walls of MOF, thus enhancing water stability, and helping preserve the porosity that is crucial for the internal diffusion of PFAS. Additionally, being a non-fluorinated ligand, it is less toxic compared to other hydrophobic, water-stable MOFs.[78,79] The fluorescence spectra of the dispersed MOF powder in water/DMF (60/40: v/v) was recorded with incremental additions of aqueous PFOA solution (Figure 3). A rapid turn-on response was observed with the addition of PFOA to the MOF suspension. The visible reddish-yellow emission was observed upon increasing the concentration of PFOA (inset of Figure 3), implying the feasibility of quick detection of PFOA by naked-eye visualization of the bright emission formation. The UV−vis spectrum of the MOF suspension was recorded after the PFOA sensing experiment and compared with the spectrum of the MOF suspension prior to PFOA addition. After PFOA sensing, the UV−vis spectra of **U-1** MOF retain about the same shape with the two prominent peaks around 543 and 496 nm slightly blue-shifted to 540 and 492 nm, respectively (Figure S16). In our sensing experiments, 490 nm (close to one of the two absorption maxima) was chosen as the

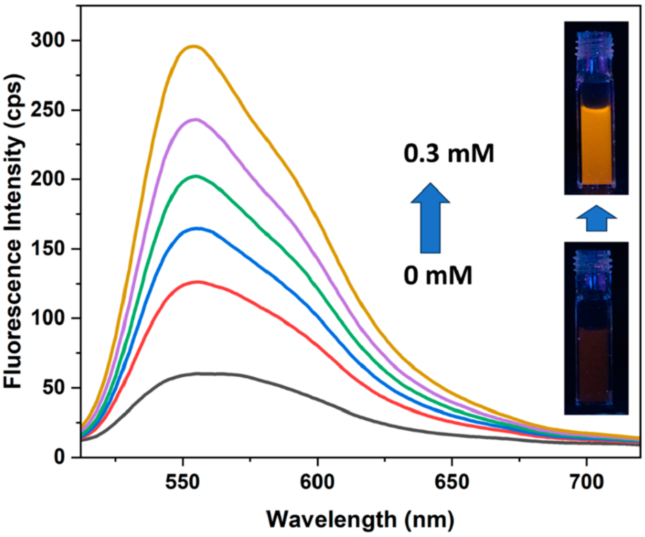

Figure 3. Fluorescence spectra of **U-1** MOF suspension (0.13 mg/mL) measured in a binary solvent of water/DMF (60/40, v/v) in the presence of increasing concentration of PFOA (excitation wavelength λex: 490 nm). Inset: naked eye visualization of the fluorescence emission change of **U-1** MOF in a cuvette in the presence of PFOA (0.3 mM).

excitation wavelength to monitor the turn-on emission in response to PFOA binding. The slight blue shift observed in the absorption spectra can be attributed to structural changes in the MOF induced by PFOA binding, as elaborated in the mechanism section. The fluorescence quantum yield of the system also increased from 0.0 to 0.02 after PFOA addition (Figure S17 and S18).[80,81]

To assess the response time of the **U-1** MOF for detecting PFOA, time-dependent experiments were carried out with various concentrations of PFOA solutions (Figure S19). For each concentration of PFOA, the emission intensity (at λ_{max} = 561 nm) of **U-1** MOF suspension was measured as a function of time after addition of PFOA. The results demonstrate that the **U-1** MOF exhibits a rapid response, taking less than 5 min to reach adsorption equilibrium with PFOA. We are aware that the sensing response time observed is relatively longer when compared to other MOF based sensors used for detection of small ions or molecules.[82,83] The relatively long response is primarily attributed to the slow diffusion of PFOA within the nanopores of MOF. The adsorption equilibrium of PFOA is determined by the complexation of the carboxylic headgroup of PFOA with the Zr(IV) ion in conjunction with the hydrophobic interaction between the fluorinated alkyl chain of PFOA and the chlorinated backbone of PDI. While the mesoporosity of MOF enhances the adsorption capacity, the spatial confinement may also limit the diffusion kinetics. This represents a typical trade-off in materials design and optimization.

To check the selectivity of **U-1** MOF toward PFOA, another common PFAS compound, PFOS, was also tested under the same conditions. Surprisingly, only a slight turn-on response was observed for PFOS (Figure 4). This is likely due to the relatively weaker complexation of the sulfonic group (compared to the carboxylic group of PFOA) with the Zr(IV) ion. Indeed, while ligands with carboxylic groups are common for the synthesis of stable MOFs, it is rare to have a MOF synthesized from sulfonic based ligands. Trifluoroacetic acid (TFA), a short chain analogue of PFOA, was also tested and demonstrated a much lower response under the same conditions compared to PFOA (Figure 4). This indicates that the long alkyl chain of PFOA plays a crucial role in the strong binding interaction with the MOF, for which the longer chains exhibit stronger hydrophobic interactions with the PDI ligand. In addition to fluorinated compounds, other long chain carboxylic acids (octanoic acid and lauric acid) and common surfactants such as cetyltrimethylammonium bromide (CTAB), were also examined for the same sensing response. These compounds have an alkyl structure similar to that of PFOA, but without fluorination. Interestingly, no significant turn-on response was observed from octanoic or lauric acid. This is likely due to the lower hydrophobicity of non-fluorinated alkyl chains, which in turn reduces the binding interaction with PDI ligands in the MOF. More remarkably, the addition of CTAB did not result in any turn-on response. Rather, it caused a slight decrease in emission intensity (Figure 4). This is not surprising when taking the positively charged headgroup of CTAB into account, which would not compete for the complexation with the metal center. Additional testing was also carried out using other fluorinated substances, namely,

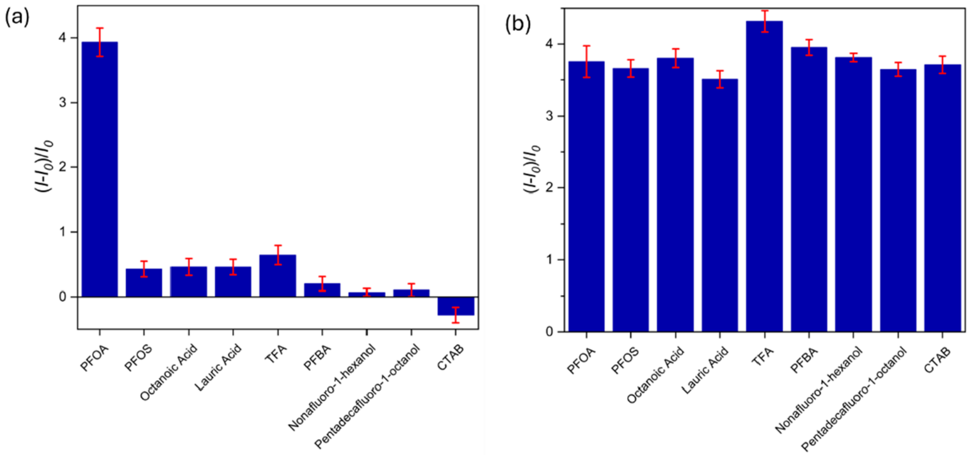

Figure 4. Bar plot showing the relative fluorescence intensity change of **U-1** MOF toward PFOA in comparison to other potential interferents as tested individually (a) and coexisting with the interferents (b). The test was performed in a binary solvent of water/DMF (60/40, v/v), and the concentration of **U-1** MOF is 0.13 mg/mL, while the concentrations of PFOA and each interferent are 0.3 mM.

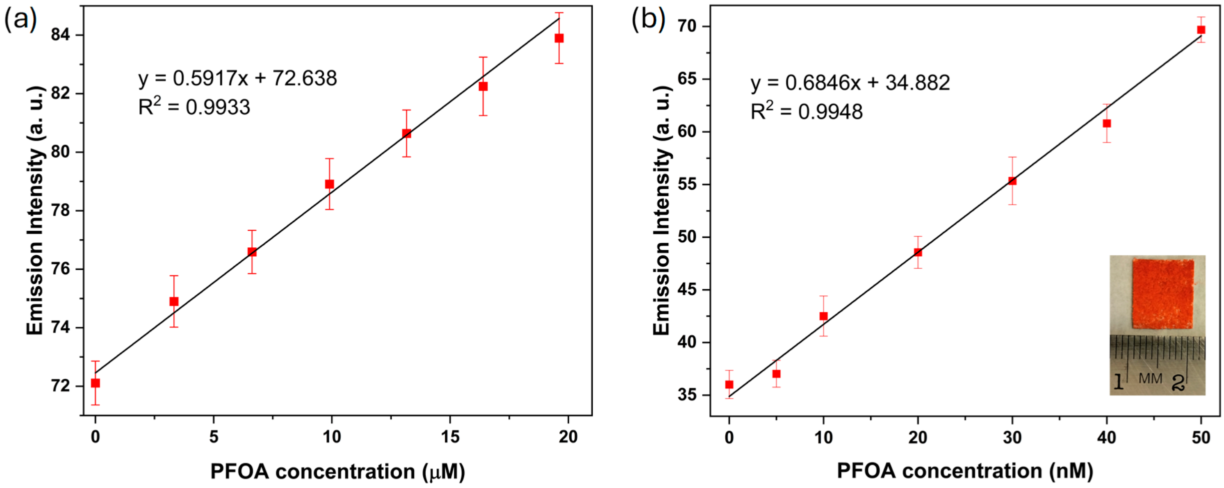

Figure 5. (a) Emission intensity measured for **U-1** MOF dispersed in water/DMF (60/40 v/v) at concentration of 0.13 mg/mL as a function of the concentration of PFOA present; (b) similar titration performed for **U-1** MOF deposited on a ∼1 × 1 cm filter paper (at a loading density of 5 mg/cm^2) upon drop-casting of different concentrations of PFOA at a fixed volume of 75 μL. (Inset: digital image of a MOF coated filter paper.).

pentafluorobenzoic acid (PFBA), 1H,1H,2H,2H-perfluoro-1-hexanol, and 1H,1H-pentadecafluoro-1-octanol. As depicted in Figure 4a, no significant turn-on response was observed from these fluorinated analytes, which further suggests the high selectivity of **U-1** MOF toward PFOA.

To further examine the sensitivity of the **U-1** MOF, we performed another set of experiments wherein the interferent compounds were added together with PFOA in equal amount. As depicted in Figure 4b, the **U-1** MOF exhibited a similar turn-on signal with no significant influence from the coexistence of interferents. The original fluorescence spectra measured for the experiments shown in Figure 4a and b are presented in Figure S20 and S21. In addition to long chain acids and surfactants, polyaromatic hydrocarbons (PAHs) and their derivates, halogenated acids and nitroaromatics are also considered a major class of water pollutants.[84] PAHs are fluorescent in nature and can give false positive responses for any turn-on sensor. The common PAHs (naphthalene, anthracene, fluorene, and pyrene) and their derivatives (e.g., 9,10-phenanthrenequinone, 2-bromofluorene) were tested along with other previously stated interferents. Interestingly, no turn-on was observed in the presence of these PAH molecules (Figure S22). This result confirms that the **U-1** MOF would not show any false turn-on responses in the presence of fluorescent PAH molecules. It is also significant that even in the presence of PAH molecules, **U-1** shows a significant turn-on response toward PFOA (Figure S23−28). A significant interference from the 2-bromofluorene molecule was observed (Figure S29). The presence of a heavy atom, in this case bromine, can quench the fluorescence of the system significantly.[85] The additional testing with halogenated acids (2,4,6- trichlorobenzoic acid and 3,5-dichlorobenzoic acid) and nitroaromatics (4-nitrophenol and 4-nitrotoluene) reveals that their presence does not significantly affect the sensing behavior of the current MOF (Figure S30 and S31). The chlorobenzoic acid does not alter the fluorescence of the MOF significantly, whereas nitroaromatics, well-known quenchers of MOF fluorescence,[86] show an insignificant amount of fluorescence quenching. More importantly, MOF shows a significant turn-on response toward PFOA even in the presence of these interferences. These findings further highlight the selectivity of **U-1** MOF toward PFOA, paving the way to application development in real practices, where multiple compounds coexist in water samples.

The sensing experiments were conducted in a mixture of water and DMF, while the PFOA analyte was introduced solely in water to examine the impact of increasing the water content in the sensing system. To assess the effect of the water content on the emission behavior, fluorescence spectra of the MOF were measured using different ratios of water to DMF in solution. As illustrated in Figure S32, there was a rapid decline in the emission intensity of the MOF with increasing water content. This observation aligns with the findings of the solvent-dependent study mentioned earlier. These results strongly suggest that the turn-on response observed in the MOF can be solely attributed to the presence of PFOA.

Reusability is a crucial parameter in sensor development, ensuring prolonged usage and cost-effectiveness. The reusability of the current MOF sensor was tested for up to five cycles following sensing experiments. After each sensing cycle, the MOF was recovered by washing with a 30/70 (v/v) binary mixture of 0.1 M HCl in methanol.[61] As illustrated in Figure S33, the MOF continues to exhibit a turn-on signal, even after five sensing cycles. The slight decrease in sensitivity observed with each cycle can be attributed to the incomplete rinsing of the adsorbed PFOA, which results in a relatively higher emission background (I_0).

To estimate the limit of detection (LOD), the emission intensity of **U-1** MOF dispersed in water/DMF (60/40 v/v) was measured at increasing concentrations of PFOA in the range 0−20 μM. As shown in Figure 5a, the emission intensity increases linearly with the concentration of PFOA within the testing concentration range, which yields a LOD of 1.68 μM following the IUPAC 3σ criterion. To further improve the LOD, we coupled the fluorescent sensing with solid phase extraction (SPE) by depositing the **U-1** MOF powder within the matrix of filter paper. The cellulose fibril network of paper provides an ideal substrate for dispersing the MOF powder and forming a stable uniform film.[87] The high porosity of MOF and cellulose substrate enables a significant SPE effect that helps concentrate the PFOA compounds from low concentration samples. This allows for detection of PFOA at much lower

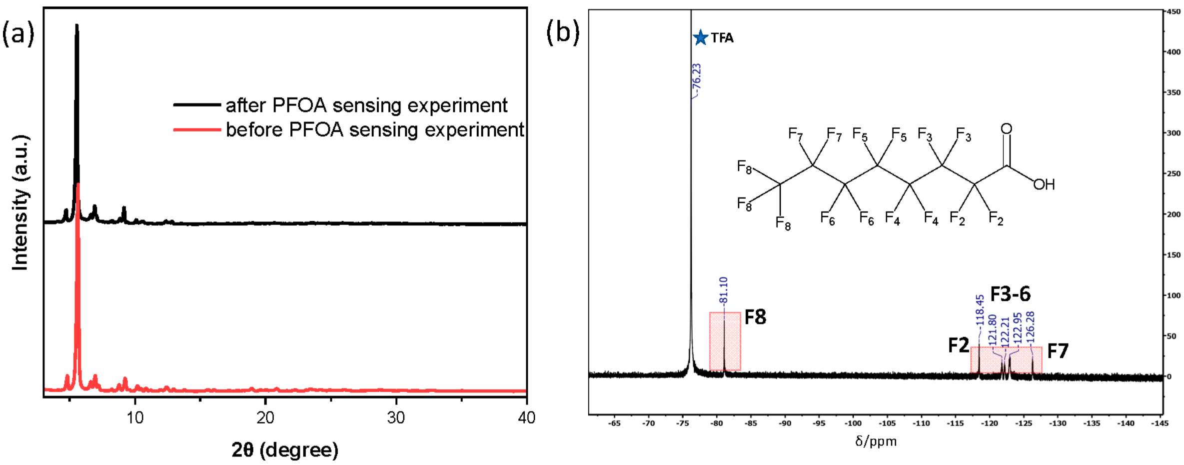

Figure 6. (a) PXRD patterns of the **U-1** MOF before and after the sensing experiment with PFOA. (b) ^{19}F NMR spectra of the digested MOF after experimentation with PFOA.

concentrations as shown in Figure 5b. From the linear relationship between the emission intensity of the MOF and the concentration of PFOA, an LOD of 3.1 nM was obtained. This low LOD is comparable with other fluorescence-based sensor materials developed recently (Table S3). For each concentration tested in Figure 5b, a total of 75 μL of aqueous solution of PFOA was slowly cast onto the MOF-coated paper so that no water extruding occurred and the evaporation of water gradually concentrated PFOA in the matrix. Depending on the evaporation temperature and time, the concentrative factor (equivalent to the volume ratio of the water before and after evaporation) can be precisely controlled, providing high measurement reproducibility. The similar SPE effect was also reported recently for a fluorescent sensor for detecting organic amines like aniline in aqueous samples, for which the LOD was also pushed down to the nM level through effective concentration by SPE.[88] The LOD in combination with low cost and simple operation, intrinsic traits of paper-based sensors, provides great potential for the MOF materials reported herein to be further developed for practical use in quick on-site detection of PFAS. Moreover, by tuning the ligand structure and binding groups, the reported approach can be extended to detection of other PFAS.

The identification of PFOA in the blood of individuals without occupational exposure to the chemical initially pointed to residential drinking water as the primary source of human exposure. Therefore, it is necessary for a PFOA sensor to be capable of operating effectively in complex, real-world systems. Sensing experiments for PFOA were conducted using tap and drinking water samples to address this need for reliability in diverse environmental matrices. The titration plot depicted in Figure S34 indicates that the MOF could detect PFOA in both drinking and tap water. The LOD was determined to be 1.73 and 2.03 μM for the drinking and tap water, respectively (Figure S35). Compared to the test with deionized water samples, the LOD obtained in drinking water remains about the same (1.68 *vs* 1.73 μM), while the LOD obtained with tap water samples is slightly higher, which us likely attributed to the presence of unidentified interferences (e.g., ions) in the tap water. Standard recovery experiments were performed, wherein PFOA solutions prepared in tap or drinking water were spiked as internal standards.[89] **U-1** suspensions were treated with three different concentrations of PFOA (5, 10, 15 μM), and the fluorescence emission intensities were recorded. The measured concentrations closely matched the spiked concentrations of PFOA, yielding recovery percentages exceeding 91% (Table S4). These promising outcomes underscore the broad scope and practical utility of the current **U-1** MOF for PFOA sensing in real-world scenarios.

Mechanisms of PFOA Binding with U-1 MOF. From the fluorescence sensing response obtained above for PFOA in comparison with other analytes, the binding of PFOA within the MOF depends on both the complexation with the metal ion and the hydrophobic interaction with the PDI ligands. The strong binding of PFAS results in conformational change of the π-conjugation structure of PDI backbone, particularly the dihedral twisting angle around the four chloro-moieties. Such conformational change in turn leads to an increase in emission intensity (*vide infra*). There remains a possibility that the intercalation of PFOA may destroy the intrinsic structure of the **U-1** MOF, thus releasing the free ligand of PDI, leading to fluorescence turn-on. To exclude this possibility, the structural integrity of **U-1** MOF powder was verified by PXRD measurements before and after the PFOA treatment. Almost no change in PXRD patterns was observed for the MOF sample after being tested with PFOA (Figure 6a), implying that the framework structure of the **U-1** MOF remained robust upon PFOA binding. The SEM image was acquired after the sensing experiments and compared with that of the MOF before PFOA sensing (Figure S36). No major changes were observed for the MOFs' shape and size, which further confirms the robustness of the MOF. Minor agglomeration of MOF particles was observed after sensing test with PFOA. The overall hydrophobicity of the MOF may have increased by PFOA adsorption during the sensing event, leading to increased hydrophobic interactions among the MOF particles and, consequently, particle agglomeration.

^{19}F-NMR spectroscopy was also used to examine any inclusion of PFOA molecules inside the MOF after the sensing experiment. The MOF was collected after the sensing experiment and then digested with tripotassium phosphate. The ^{19}F NMR spectrum of the digested MOF was recorded and compared with pure PFOA. As depicted in Figure 6b, the digested MOF shows a ^{19}F NMR pattern about the same as that obtained from pure PFOA (Figure S37), for which the peaks from −118.3 to −126.2 ppm correspond to the fluorine atoms attached to C2−C7 carbons, and the peak near −81.0 ppm corresponds to chemical shifting of the terminal − CF_3

functional group.[90] The similarity in the ^{19}F NMR pattern confirms the inclusion of PFOA into the MOF during the sensing test. An additional peak observed at −76.2 ppm in Figure 6b suggests the presence of TFA molecules, which were used as modulator for the synthesis of **U-1** MOF.

XPS was employed to analyze the surface changes of the **U-1** MOF upon PFOA adsorption. The XPS survey scans of **U-1** MOF before and after test with PFOA, and pure PFOA are shown in Figure S38, with the data of Zr 3d and F 1s binding energies summarized in Table S3. The analysis reveals that **U-1** MOF has characteristic Zr 3d peaks located at 183.71 and 186.11 eV, indicating the presence of Zr^{4+}.[91] Moreover, the F 1s binding energies of the MOF were found to be at 689.0 and 687 eV. Upon adsorption with PFOA, a shift in the F 1s binding energies was observed, with values of 688.91 and 685.60 eV, which agrees with the chemical changes induced in the trifluoromethyl groups due to adsorption in the MOF. Interestingly, the characteristic Zr 3d binding energies also shifted from 183.71 and 186.11 eV to 184.05 and 186.30 eV, respectively, indicating a perturbation in the coordination environment induced by PFOA binding.[91] Binding to a fluorinated compound causes the loss of electron density over zirconium, which in turn increases its $3d_{3/2}$ and $3d_{5/2}$ binding energies in the MOF.[92] All of the data presented confirm the successful adsorption of PFOA into the MOF.

The fluorinated hydrophobic chain, along with a polar carboxylic acid group, plays a pivotal role for the selective sensing of PFOA. An additional fluorescence experiment was performed to support this hypothesis. A series of short-chain perfluoroalkyl carboxylic acids (PFCAs) were treated with **U-1** MOF suspension and changes in emission spectra were recorded. As depicted in Figure S39, the trifluoroacetic acid and shortened fluoroalkyl carboxylic acid show minimal responses. However, a steady increase in turn-on signal was found with increasing the length of fluoroalkyl chain. This confirms that the sensing response is dependent on both the hydrophobic chain and polar carboxylate functional group of PFCAs.

Computational Modeling of PFOA@U-1 Interactions. Increasing binding affinity for longer-chain perfluoroalkyl carboxylic acids (PFCAs) compared with short chain PFCAs was observed in **U-1**. A combined experimental and theoretical study was undertaken to understand the molecular-level interactions between MOF and PFOA, aiming to gain insights into the sensing mechanism. It is known that PFOA exhibits significantly stronger acidity than its corresponding fatty acid, implying that the interaction between PFOA and MOF could entail a covalent interaction. The shift in Bragg diffraction peak positions toward lower 2θ values after PFOA sensing was confirmed by PXRD analysis (Figure S40). This low-angle shift suggests an increase in cell volume after PFOA interaction.[93] To confirm this change, a Pawley refinement was attempted postsensing. The new model was constructed by replacing coordinating TFA molecules with PFOA. The asymmetric unit of PFOA@**U-1** contains two crystallographically independent Zr atoms, one $\mathbf{L}^{2-}$ ligand molecule, one PFOA molecule and two μ_3-O atoms (Figure S41). The results of Pawley refinement revealed that the simulated and experimental PXRD data were identical for the PFOA@**U-1** system (Figure S42 and table S6), with the cell volume expanded to 2.7%. Notably, the highly twisted PDI backbone with a dihedral twisting angle ∠(C−C−C−C) of 36.9° was drastically reduced to 26.4°after the incorporation of PFOA (Figure S43). The PFOA-induced fluorescence turn-on can be explained by the relaxation of the twisted structure of the perylene core. The increased dihedral angle of the $H_2\mathbf{L}$ ligand found in the **U-1** MOF results in a reduced effectiveness of the overlap between the p orbital and the sp^2 hybridized orbital. This decreased overlap with the p orbital leads to a breakdown of conjugation within the ligand, ultimately resulting in fluorescence quenching.[94−96] Conversely, after the coordinating interaction of PFOA with **U-1**, the MOF underwent structural changes at the molecular level, and the perylene core attained more planarity in geometry. Through this, a more conjugated state is achieved. Such a change in the perylene core is likely responsible for the restoration of fluorescence and the observed turn-on response.

DFT calculations were further employed to investigate the origin of interactions of PFOA with the MOF. PFOA molecules were introduced at the adsorption sites (Zr_6 SBU) in a model of **U-1** that was previously identified and confirmed by XPS and X-ray structure refinement. The resulting optimized structure of PFOA@**U-1** is displayed in Figure S44. The Zr_6 node at the adsorption site features a Zr-coordinated TFA molecule that enables hydrogen bonding interactions with PFOA via − CF_3 functional groups, while Zr sites promote additional coordinative bonding. The adsorption of PFOA near the Zr_6 node is visualized in Figure 7, showing that the PFOA@**U-1** system is stabilized by strong H-bonding interactions (RCOOH···F−C, 1.97 Å), accompanied by strong coordinate bonding (RCOOH−Zr, 2.18 Å). Such strong coordinate bonding is in line with the proposed complex formation mechanism as derived from experimental data.

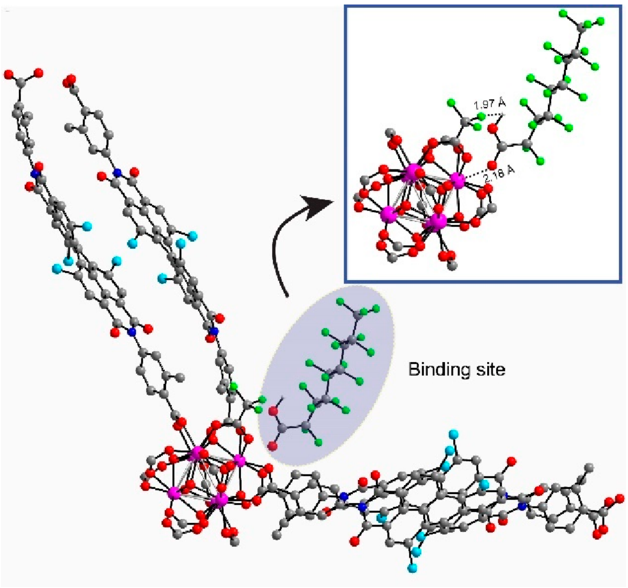

Figure 7. DFT-optimized geometries of the PFOA−PDI ligand−Zr_6 node domains within PFOA@**U-1** are depicted at the adsorption site. Additionally, a zoomed-in view of the respective adsorption site shows dashed lines representing hydrogen bonding and covalent interactions of the RCOOH···F−C and RCOOH−Zr_6 motifs, respectively.

■ CONCLUSION

In summary, we report on the synthesis and systematic exploration of a robust, fluorescent PDI-based MOF, namely, **U-1**, for the detection of PFOA through a fluorescence turn-on response. Our findings reveal that **U-1** MOF exhibits outstanding stability in various chemical environments. The fluorescent sensing of **U-1** MOF is relatively selective toward PFOA when tested in the solution phase. The same fluorescence turn-on response was also observed for the solid phase by depositing the MOF onto a filter paper. Built upon the effective SPE effect, the LOD of the sensor film was decreased to 3.1 nM. Detailed structural analysis suggests that the fluorescence turn-on is predominated by two cooperative interactions, the complexation between the carboxylic group of PFOA and the zirconium metal center, and the hydrophobic interaction between the fluorinated alkyl chain of PFOA and the PDI ligand. The work presented herein showcases the great potential of PDI-based MOFs as fluorescent probes for the sensitive and selective detection of PFAS, for which the detection selectivity can be further improved by tuning the ligand structure and the porosity of MOFs.

■ ASSOCIATED CONTENT

Supporting Information

The Supporting Information is available free of charge at https://pubs.acs.org/doi/10.1021/acsami.4c03389.

> Synthesis details for ligand, PXRD patterns, TGA curves, N_2 sorption isotherms, fluorescence spectra, NMR, SEM images, mass and ATR-IR spectra, crystal structure information (PDF)

■ AUTHOR INFORMATION

Corresponding Author

Ling Zang − *Nano Institute of Utah, and Department of Materials Science and Engineering, University of Utah, Salt Lake City, Utah 84112, United States;* orcid.org/0000-0002-4299-0992; Email: lzang@eng.utah.edu

Authors

Rana Dalapati − *Nano Institute of Utah, and Department of Materials Science and Engineering, University of Utah, Salt Lake City, Utah 84112, United States*

Matthew Hunter − *Nano Institute of Utah, and Department of Materials Science and Engineering, University of Utah, Salt Lake City, Utah 84112, United States*

Mostakim SK − *Lab of Soft Interfaces, Department of Metallurgical Engineering and Materials Science, Indian Institute of Technology Bombay, Mumbai 400076, India*

Xiaomei Yang − *Nano Institute of Utah, and Department of Materials Science and Engineering, University of Utah, Salt Lake City, Utah 84112, United States*

Complete contact information is available at: https://pubs.acs.org/10.1021/acsami.4c03389

Author Contributions

The manuscript was written through contributions of all authors

Funding

This work was sponsored by Gentex Corporation under award #10060686.

Notes

The authors declare the following competing financial interest(s): Ling Zang has a significant financial interest in Gentex Corporation, which funded this research.

■ ACKNOWLEDGMENTS

The authors are very grateful to Gentex Corporation for sponsorship of the research, and University of Utah for instrumental facilities and other support.

■ REFERENCES

(1) Ali, M.; Meaney, S. P.; Giles, L. W.; Holt, P.; Majumder, M.; Tabor, R. F. Capture of perfluorooctanoic acid using oil-filled graphene oxide−silica hybrid capsules. *Environ. Sci. Technol.* **2020**, *54*, 3549−3558.

(2) Thomaidi, V.; Tsahouridou, A.; Matsoukas, C.; Stasinakis, A.; Petreas, M.; Kalantzi, O. Risk assessment of PFASs in drinking water using a probabilistic risk quotient methodology. *Sci. Total Environ.* **2020**, *712*, 136485.

(3) Herzke, D.; Olsson, E.; Posner, S. Perfluoroalkyl and polyfluoroalkyl substances (PFASs) in consumer products in Norway−A pilot study. *Chemosphere* **2012**, *88*, 980−987.

(4) Boston, C. M.; Banacos, N.; Heiger-Bernays, W. Per-and polyfluoroalkyl substances: A national priority for safe drinking water. *Public Health Rep.* **2019**, *134*, 112−117.

(5) Cordner, A.; De La Rosa, V. Y.; Schaider, L. A.; Rudel, R. A.; Richter, L.; Brown, P. Guideline levels for PFOA and PFOS in drinking water: the role of scientific uncertainty, risk assessment decisions, and social factors. *J. Exposure Sci. Environ. Epidemiol.* **2019**, *29*, 157−171.

(6) Post, G. B. Recent US state and federal drinking water guidelines for per-and polyfluoroalkyl substances. *Environ. Toxicol. Chem.* **2021**, *40*, 550−563.

(7) Anderko, L.; Pennea, E. Exposures to per-and polyfluoroalkyl substances (PFAS): Potential risks to reproductive and children's health. *Curr. Probl. Pediatr. Adolesc. Health Care* **2020**, *50*, 100760.

(8) Lanza, H. A.; Cochran, R. S.; Mudge, J. F.; Olson, A. D.; Blackwell, B. R.; Maul, J. D.; Salice, C. J.; Anderson, T. A. Temporal monitoring of perfluorooctane sulfonate accumulation in aquatic biota downstream of historical aqueous film forming foam use areas. *Environ. Toxicol. Chem.* **2017**, *36*, 2022−2029.

(9) Anderson, R. H.; Long, G. C.; Porter, R. C.; Anderson, J. K. Occurrence of select perfluoroalkyl substances at US Air Force aqueous film-forming foam release sites other than fire-training areas: Field-validation of critical fate and transport properties. *Chemosphere* **2016**, *150*, 678−685.

(10) Boisvert, G.; Sonne, C.; Rigét, F. F.; Dietz, R.; Letcher, R. J. Bioaccumulation and biomagnification of perfluoroalkyl acids and precursors in East Greenland polar bears and their ringed seal prey. *Environ. Pollut.* **2019**, *252*, 1335−1343.

(11) Cheng, H.; Lv, C.; Li, J.; Wu, D.; Zhan, X.; Song, Y.; Zhao, N.; Jin, H. Bioaccumulation and biomagnification of emerging poly-and perfluoroalkyl substances in marine organisms. *Sci. Total Environ.* **2022**, *851*, 158117.

(12) Kelly, B. C.; Ikonomou, M. G.; Blair, J. D.; Surridge, B.; Hoover, D.; Grace, R.; Gobas, F. A. Perfluoroalkyl contaminants in an Arctic marine food web: trophic magnification and wildlife exposure. *Environ. Sci. Technol.* **2009**, *43*, 4037−4043.

(13) De Silva, A. O.; Armitage, J. M.; Bruton, T. A.; Dassuncao, C.; Heiger Bernays, W.; Hu, X. C.; Karrman, A.; Kelly, B.; Ng, C.; Robuck, A.; Sun, M.; Webster, T. F.; Sunderland, E. M. PFAS exposure pathways for humans and wildlife: a synthesis of current knowledge and key gaps in understanding. *Environ. Toxicol. Chem.* **2021**, *40*, 631−657.

(14) Cao, Y.; Ng, C. Absorption, distribution, and toxicity of per-and polyfluoroalkyl substances (PFAS) in the brain: a review. *Environ. Sci.: Processes Impacts* **2021**, *23*, 1623−1640.

(15) Piva, E.; Fais, P.; Cecchetto, G.; Montisci, M.; Viel, G.; Pascali, J. P. Determination of perfluoroalkyl substances (PFAS) in human hair by liquid chromatography-high accurate mass spectrometry (LC-QTOF). *J. Chromatogr. B* **2021**, *1172*, 122651.

(16) Benskin, J. P.; Bataineh, M.; Martin, J. W. Simultaneous characterization of perfluoroalkyl carboxylate, sulfonate, and sulfona-

mide isomers by liquid chromatography– tandem mass spectrometry. *Anal. Chem.* **2007**, *79*, 6455−6464.

(17) Kidd, J.; Fabricatore, E.; Jackson, D. Current and future federal and state sampling guidance for per-and polyfluoroalkyl substances in environmental matrices. *Sci. Total Environ.* **2022**, *836*, 155523.

(18) Ryu, H.; Li, B.; De Guise, S.; McCutcheon, J.; Lei, Y. Recent progress in the detection of emerging contaminants PFASs. *J. Hazard. Mater.* **2021**, *408*, 124437.

(19) Dodds, J. N.; Alexander, N. L. M.; Kirkwood, K. I.; Foster, M. R.; Hopkins, Z. R.; Knappe, D. R.; Baker, E. S. From pesticides to per- and polyfluoroalkyl substances: an evaluation of recent targeted and untargeted mass spectrometry methods for xenobiotics. *Anal. chem.* **2021**, *93*, 641−656.

(20) Cennamo, N.; D'Agostino, G.; Porto, G.; Biasiolo, A.; Perri, C.; Arcadio, F.; Zeni, L. A molecularly imprinted polymer on a plasmonic plastic optical fiber to detect perfluorinated compounds in water. *Sensors* **2018**, *18*, 1836.

(21) Rodriguez, K. L.; Hwang, J.-H.; Esfahani, A. R.; Sadmani, A.; Lee, W. H. Recent developments of PFAS-detecting sensors and future direction: a review. *Micromachines* **2020**, *11*, 667.

(22) Clark, R. B.; Dick, J. E. Towards deployable electrochemical sensors for per-and polyfluoroalkyl substances (PFAS). *Chem. Commun.* **2021**, *57*, 8121−8130.

(23) Sunantha, G.; Vasudevan, N. A method for detecting perfluorooctanoic acid and perfluorooctane sulfonate in water samples using genetically engineered bacterial biosensor. *Sci. Total Environ.* **2021**, *759*, 143544.

(24) Liang, J.; Deng, X.; Tan, K. An eosin Y-based "turn-on" fluorescent sensor for detection of perfluorooctane sulfonate. *Spectrochim. Acta, Part A* **2015**, *150*, 772−777.

(25) Cheng, Z.; Du, L.; Zhu, P.; Chen, Q.; Tan, K. An erythrosin B-based "turn on" fluorescent sensor for detecting perfluorooctane sulfonate and perfluorooctanoic acid in environmental water samples. *Spectrochim. Acta, Part A* **2018**, *201*, 281−287.

(26) Lei, S.-N.; Cong, H. Fluorescence detection of perfluorooctane sulfonate in water employing a tetraphenylethylene-derived dual macrocycle BowtieCyclophane. *Chin. Chem. Lett.* **2022**, *33*, 1493−1496.

(27) Zhang, Q.; Liao, M.; Xiao, K.; Zhuang, K.; Zheng, W.; Yao, Z. A water-soluble fluorescence probe based on perylene diimide for rapid and selective detection of perfluorooctane sulfonate in 100% aqueous media. *Sens. Actuators, B* **2022**, *350*, 130851.

(28) Cheng, Z.; Dong, H.; Liang, J.; Zhang, F.; Chen, X.; Du, L.; Tan, K. Highly selective fluorescent visual detection of perfluorooctane sulfonate via blue fluorescent carbon dots and berberine chloride hydrate. *Spectrochim. Acta, Part A* **2019**, *207*, 262−269.

(29) Li, J.; Zhang, C.; Yin, M.; Zhang, Z.; Chen, Y.; Deng, Q.; Wang, S. Surfactant-sensitized covalent organic frameworks-functionalized lanthanide-doped nanocrystals: an ultrasensitive sensing platform for perfluorooctane sulfonate. *ACS omega* **2019**, *4*, 15947−15955.

(30) Liu, Q.; Huang, A.; Wang, N.; Zheng, G.; Zhu, L. Rapid fluorometric determination of perfluorooctanoic acid by its quenching effect on the fluorescence of quantum dots. *J. Lumin.* **2015**, *161*, 374−381.

(31) Zheng, Z.; Yu, H.; Geng, W.-C.; Hu, X.-Y.; Wang, Y.-Y.; Li, Z.; Wang, Y.; Guo, D.-S. Guanidinocalix [5] arene for sensitive fluorescence detection and magnetic removal of perfluorinated pollutants. *Nat. Commun.* **2019**, *10*, 1−9.

(32) Chen, Z.; Lu, Y.-L.; Wang, L.; Xu, J.; Zhang, J.; Xu, X.; Cheng, P.; Yang, S.; Shi, W. Efficient Recognition and Removal of Persistent Organic Pollutants by a Bifunctional Molecular Material. *J. Am. Chem. Soc.* **2023**, *2023* (145), 260−267.

(33) Cui, Y.; Yue, Y.; Qian, G.; Chen, B. Luminescent functional metal−organic frameworks. *Chem. Rev.* **2012**, *112*, 1126−1162.

(34) Kreno, L. E.; Leong, K.; Farha, O. K.; Allendorf, M.; Van Duyne, R. P.; Hupp, J. T. Metal−organic framework materials as chemical sensors. *Chem. Rev.* **2012**, *112*, 1105−1125.

(35) Pal, T. K. Metal−organic framework (MOF)-based fluorescence "turn-on" sensors. *Mater. Chem. Front.* **2023**, *7*, 405−441.

(36) Chongdar, S.; Mondal, U.; Chakraborty, T.; Banerjee, P.; Bhaumik, A. A Ni-MOF as fluorescent/electrochemical dual probe for ultrasensitive detection of picric acid from aqueous media. *ACS Appl. Mater. Interfaces* **2023**, *15*, 14575−14586.

(37) Wang, M.; Guo, L.; Cao, D. Metal-organic framework as luminescence turn-on sensor for selective detection of metal ions: Absorbance caused enhancement mechanism. *Sens. Actuators, B* **2018**, *256*, 839−845.

(38) Li, H.-Y.; Zhao, S.-N.; Zang, S.-Q.; Li, J. Functional metal−organic frameworks as effective sensors of gases and volatile compounds. *Chem. Soc. Rev.* **2020**, *49*, 6364−6401.

(39) Zhang, L.; Kang, Z.; Xin, X.; Sun, D. Metal−organic frameworks based luminescent materials for nitroaromatics sensing. *CrystEngComm* **2016**, *18*, 193−206.

(40) Hu, Z.; Deibert, B. J.; Li, J. Luminescent metal−organic frameworks for chemical sensing and explosive detection. *Chem. Soc. Rev.* **2014**, *43*, 5815−5840.

(41) Dong, J.; Zhao, D.; Lu, Y.; Sun, W.-Y. Photoluminescent metal−organic frameworks and their application for sensing biomolecules. *J. Mater. Chem. A* **2019**, *7*, 22744−22767.

(42) Zhang, Q.; Wang, C.-F.; Lv, Y.-K. Luminescent switch sensors for the detection of biomolecules based on metal−organic frameworks. *Analyst* **2018**, *143*, 4221−4229.

(43) Mondal, U.; Bej, S.; Hazra, A.; Mandal, S.; Pal, T. K.; Banerjee, P. Amine-substituent induced highly selective and rapid "turn-on" detection of carcinogenic 1, 4-dioxane from purely aqueous and vapour phase with novel post-synthetically modified d 10-MOFs. *Dalton Trans.* **2022**, *51*, 2083−2093.

(44) Cai, D.; Guo, H.; Wen, L.; Liu, C. Fabrication of hierarchical architectures of Tb-MOF by a "green coordination modulation method" for the sensing of heavy metal ions. *CrystEngComm* **2013**, *15*, 6702−6708.

(45) Du, T.; Wang, J.; Zhang, L.; Wang, S.; Yang, C.; Xie, L.; Liu, Z.; Ni, Y.; Xie, X.; Sun, J.; Zhang, W.; Wang, J. Missing-linker engineering of Eu (III)-doped UiO-MOF for enhanced detection of heavy metal ions. *Chem. Eng. J.* **2022**, *431*, 134050.

(46) Hazra, A.; Mondal, U.; Mandal, S.; Banerjee, P. Advancement in functionalized luminescent frameworks and their prospective applications as inkjet-printed sensors and anti-counterfeit materials. *Dalton Trans.* **2021**, *50*, 8657−8670.

(47) Cheng, W.; Tang, X.; Zhang, Y.; Wu, D.; Yang, W. Applications of metal-organic framework (MOF)-based sensors for food safety: Enhancing mechanisms and recent advances. *Trends Food Sci. Technol.* **2021**, *112*, 268−282.

(48) Raja Lakshmi, P.; Nanjan, P.; Kannan, S.; Shanmugaraju, S. Recent advances in luminescent metal−organic frameworks (LMOFs) based fluorescent sensors for antibiotics. *Coord. Chem. Rev.* **2021**, *435*, 213793.

(49) Monnier, V.; Odobel, F.; Diring, S. Exploring the Impact of Successive Redox Events in Thin Films of Metal−Organic Frameworks: An Absorptiometric Approach. *J. Am. Chem. Soc.* **2023**, *145*, 19232−19242.

(50) Chen, B.; Yang, Z.; Qu, X.; Zheng, S.; Yin, D.; Fu, H. Screening and Discrimination of Perfluoroalkyl Substances in Aqueous Solution Using a Luminescent Metal−Organic Framework Sensor Array. *ACS Appl. Mater. Interfaces* **2021**, *13*, 47706−47716.

(51) Datar, A.; Balakrishnan, K.; Zang, L. One-dimensional self-assembly of a water soluble perylene diimide molecule by pH triggered hydrogelation. *Chem. Commun.* **2013**, *49*, 6894−6896.

(52) Chen, S.; Slattum, P.; Wang, C.; Zang, L. Self-assembly of perylene imide molecules into 1D nanostructures: methods, morphologies, and applications. *Chem. Rev.* **2015**, *115*, 11967−11998.

(53) Kim, Y.-J.; Lee, Y.; Park, K.; Ahn, C. W.; Jung, H.-T.; Jeon, H.-J. Hierarchical self-assembly of perylene diimide (PDI) crystals. *J. Phys. Chem. Lett.* **2020**, *11*, 3934−3940.

(54) Zhao, Y.; Liu, T.; Gao, J.; Zhang, Q.; Liao, M.; Cheng, H.; Tian, J.; Yao, Z. Nanoassemblies Based on a Cationic Perylene Diimide Derivative and Sodium Dodecyl Sulfate: A Simple

Fluorescent Platform for Efficient Analysis of Aflatoxin B1. *Anal. Chem.* **2023**, *95*, 8250−8257.

(55) Turner, S.; Shevitski, B.; Long, H.; Lorenzo, M.; Marquez, J.; Aloni, S.; Altoe, V.; Worsley, M. A.; Zettl, A. Self-assembly and metal-directed assembly of organic semiconductor aerogels and conductive carbon nanofiber aerogels with controllable nanoscale morphologies. *Carbon* **2019**, *153*, 648−656.

(56) Ding, H.; Wang, Z.; Kong, K.; Feng, S.; Xu, L.; Ye, H.; Wu, W.; Gong, X.; Hua, J. Efficient and stable photocatalytic H 2 evolution by self-assembly of zirconium (iv) coordination with perylene diimide supramolecules under visible light irradiation. *J. Mater. Chem. A* **2021**, *9*, 7675−7683.

(57) Keum, C.; Lee, H.; Kwon, C.; Han, B.; Lee, S.-Y. Metal-induced self-assembly template for controlled growth of ZIF-8 nanorods. *Chem. Mater.* **2020**, *32*, 7941−7950.

(58) Lü, B.; Chen, Y.; Li, P.; Wang, B.; Müllen, K.; Yin, M. Stable radical anions generated from a porous perylenediimide metal-organic framework for boosting near-infrared photothermal conversion. *Nat. Commun.* **2019**, *10*, 1−8.

(59) Goswami, S.; Rimoldi, M.; Anderson, R.; Lee, C.; Li, X.; Li, A.; Deria, P.; Chen, L. X.; Schaller, R. D.; Gomez-Gualdron, D. A.; Farha, O. K.; Hupp, J. T. Toward Ideal Metal−Organic Framework Thin-Film Growth via Automated Layer-by-Layer Deposition: Examples Based on Perylene Diimide Linkers. *Chem. Mater.* **2022**, *34*, 9446−9454.

(60) Chen, H.; Zeng, W.; Liu, Y.; Dong, W.; Cai, T.; Tang, L.; Li, J.; Li, W. Unique MIL-53 (Fe)/PDI supermolecule composites: Z-scheme heterojunction and covalent bonds for uprating photocatalytic performance. *ACS Appl. Mater. Interfaces* **2021**, *13*, 16364−16373.

(61) Li, R.; Alomari, S.; Stanton, R.; Wasson, M. C.; Islamoglu, T.; Farha, O. K.; Holsen, T. M.; Thagard, S. M.; Trivedi, D. J.; Wriedt, M. Efficient removal of per-and polyfluoroalkyl substances from water with zirconium-based metal−organic frameworks. *Chem. Mater.* **2021**, *33*, 3276−3285.

(62) Li, R.; Alomari, S.; Islamoglu, T.; Farha, O. K.; Fernando, S.; Thagard, S. M.; Holsen, T. M.; Wriedt, M. Systematic study on the removal of per-and polyfluoroalkyl substances from contaminated groundwater using metal−organic frameworks. *Environ. Sci. Technol.* **2021**, *55*, 15162−15171.

(63) WinXPOW*version 2.11 2005.11* DOI: 10.1177/1077800404273415

(64) *Materials Studio Software Package v5.0*; Accelrys Inc.: San Diego, 2009.

(65) Nandi, S.; Banesh, S.; Trivedi, V.; Biswas, S. A dinitro-functionalized metal−organic framework featuring visual and fluorogenic sensing of H 2 S in living cells, human blood plasma and environmental samples. *Analyst* **2018**, *143*, 1482−1491.

(66) Pal, P.; Rastogi, S. K.; Gibson, C. M.; Aston, D. E.; Branen, A. L.; Bitterwolf, T. E. Fluorescence sensing of zinc (II) using ordered mesoporous silica material (MCM-41) functionalized with N-(quinolin-8-yl)-2-[3-(triethoxysilyl) propylamino] acetamide. *ACS Appl. Mater. Interfaces* **2011**, *3*, 279−286.

(67) Zang, L.; Che, Y.; Moore, J. S. One-dimensional self-assembly of planar π-conjugated molecules: adaptable building blocks for organic nanodevices. *Acc. Chem. Res.* **2008**, *41*, 1596−1608.

(68) Würthner, F.; Saha-Möller, C. R.; Fimmel, B.; Ogi, S.; Leowanawat, P.; Schmidt, D. Perylene bisimide dye assemblies as archetype functional supramolecular materials. *Chem. Rev.* **2016**, *116*, 962−1052.

(69) Zang, L. Interfacial donor−acceptor engineering of nanofiber materials to achieve photoconductivity and applications. *Acc. Chem. Res.* **2015**, *48*, 2705−2714.

(70) Chen, S.; Xue, Z.; Gao, N.; Yang, X.; Zang, L. Perylene diimide-based fluorescent and colorimetric sensors for environmental detection. *Sensors* **2020**, *20*, 917.

(71) Zhang, M.; Shi, J.; Liao, C.; Tian, Q.; Wang, C.; Chen, S.; Zang, L. Perylene imide-based optical chemosensors for vapor detection. *Chemosensors* **2021**, *9*, 1.

(72) Chen, S.; Zhou, M.; Zhu, L.; Yang, X.; Zang, L. Architectures and Mechanisms of Perylene Diimide-Based Optical Chemosensors for pH Probing. *Chemosensors* **2023**, *11*, 293.

(73) Hu, Z.; Deibert, B. J.; Li, J. Luminescent metal−organic frameworks for chemical sensing and explosive detection. *Chem. Soc. Rev.* **2014**, *43*, 5815−5840.

(74) Dalapati, R.; Hunter, M.; Zang, L. A Dual Fluorometric and Colorimetric Sulfide Sensor Based on Coordinating Self-Assembled Nanorods: Applicable for Monitoring Meat Spoilage. *Chemosensors* **2022**, *10*, 500.

(75) Kim, W.; Nowak-Król, A.; Hong, Y.; Schlosser, F.; Würthner, F.; Kim, D. Solvent-modulated charge-transfer resonance enhancement in the excimer state of a bay-substituted perylene bisimide cyclophane. *J. Phys. Chem. Lett.* **2019**, *10*, 1919−1927.

(76) Sadeghianlemraski, M.; Harding, C. R.; Welch, G. C.; Aziz, H. Significant Photostability Enhancement of Inverted Organic Solar Cells by Inserting an N-Annulated Perylene Diimide (PDIN-H) between the ZnO Electron Extraction Layer and the Organic Active Layer. *ACS Appl. Energy Mater.* **2020**, *3*, 11655−11665.

(77) Li, C.; Gao, Y.; Huang, R.; Fang, L.; Sun, Y.; Yang, Y.; Gou, S.; Zhao, J. An effective supramolecular approach to boost the photodynamic therapy efficacy of a near-infrared activating perylene diimide-based photosensitizer. *ACS Materials Lett.* **2022**, *4*, 657−664.

(78) Yan, L.; Zheng, H.-T.; Song, L.; Wei, Z.-W.; Jiang, J.-J.; Su, C.-Y. Microporous Fluorinated MOF with Multiple Adsorption Sites for Efficient Recovery of C2H6 and C3H8 from Natural Gas. *ACS Appl. Mater. Interfaces* **2024**, *16*, 6579−6588.

(79) Noro, S.-i.; Nakamura, T. Fluorine-functionalized metal−organic frameworks and porous coordination polymers. *NPG Asia Mater.* **2017**, *9*, e433−e433.

(80) Kandi, D.; Mansingh, S.; Behera, A.; Parida, K. Calculation of relative fluorescence quantum yield and Urbach energy of colloidal CdS QDs in various easily accessible solvents. *J. Lumin.* **2021**, *231*, 117792.

(81) Mondal, A.; Hazra, A.; Chattopadhyay, M. K.; Kundu, D.; Tarai, S. K.; Biswas, P.; Bhattacharjee, A.; Mandal, S.; Banerjee, P. Explicating the recognition phenomenon of hazardous nitro-aromatic compound from contaminated environmental and cellular matrices by rationally designed pyridine-functionalized molecular probes. *Heliyon* **2023**, *9*, e13620.

(82) Wu, T.; Gao, X.-j.; Ge, F.; Zheng, H. - g. Metal−organic frameworks (MOFs) as fluorescence sensors: principles, development and prospects. *CrystEngComm* **2022**, *24*, 7881−7901.

(83) Li, T.; Zhu, X.; Hai, X.; Bi, S.; Zhang, X. Recent Progress in Sensor Arrays: From Construction Principles of Sensing Elements to Applications. *ACS Sens.* **2023**, *8*, 994−1016.

(84) Adeola, A. O.; Forbes, P. B. Advances in water treatment technologies for removal of polycyclic aromatic hydrocarbons: Existing concepts, emerging trends, and future prospects. *Water Environ. Res.* **2021**, *93*, 343−359.

(85) de Foresta, B.; Gallay, J.; Sopkova, J.; Champeil, P.; Vincent, M. Tryptophan octyl ester in detergent micelles of dodecylmaltoside: fluorescence properties and quenching by brominated detergent analogs. *Biophys. J.* **1999**, *77*, 3071−3084.

(86) Dalapati, R.; Biswas, S. Post-synthetic modification of a metal-organic framework with fluorescent-tag for dual naked-eye sensing in aqueous medium. *Sens. Actuators, B* **2017**, *239*, 759−767.

(87) Xu, M.; Bunes, B. R.; Zang, L. based vapor detection of hydrogen peroxide: colorimetric sensing with tunable interface. *ACS Appl. Mater. Interfaces* **2011**, *3*, 642−647.

(88) Zhang, M.; Dalapati, R.; Shi, J.; Liao, C.; Tian, Q.; Wang, C.; Yang, X.; Chen, S.; Porter, M. D.; Zang, L. Fluorescent sensor based on solid-phase extraction with negligible depletion: A proof-of-concept study with amines as analytes. *Anal. Chim. Acta* **2023**, *1245*, 340828.

(89) Kanwal, T.; Rasheed, S.; Hassan, M.; Fatima, B.; Xiao, H.-M.; Musharraf, S. G.; Najam-ul-Haq, M.; Hussain, D. Smartphone-Assisted EY@ MOF-5-Based Dual-Emission Fluorescent Sensor for

Rapid On-Site Detection of Daclatasvir and Nitenpyram. *ACS Appl. Mater. Interfaces* **2024**, *16*, 1688−1704.

(90) Ning, C.; Ma, H.; Pedersen, C. M.; Chang, H.; Wang, Y.; Qiao, Y. Interaction between environmental contaminant PFOA and PAMAM in water: ^{19}F and ^{1}H NMR studies. *J. Mol. Liq.* **2019**, *283*, 45−50.

(91) Li, Q.; Zhu, H.; Tang, Y.; Zhu, P.; Ma, H.; Ge, C.; Yan, F. Chemically grafting nanoscale UIO-66 onto polypyrrole nanotubes for long-life lithium−sulfur batteries. *Chem. Commun.* **2019**, *55*, 12108−12111.

(92) Wang, J.; Lin, X.; Luo, X.; Long, Y. A sorbent of carboxymethyl cellulose loaded with zirconium for the removal of fluoride from aqueous solution. *Chem. Eng. J.* **2014**, *252*, 415−422.

(93) Robertson, G. P.; Mosca, S.; Castillo-Blas, C.; Son, F. A.; Farha, O. K.; Keen, D. A.; Anzellini, S.; Bennett, T. D. Survival of Zirconium-Based Metal−Organic Framework Crystallinity at Extreme Pressures. *Inorg. Chem.* **2023**, *62*, 10092−10099.

(94) He, Q.; Dong, F.; Xing, L.; He, H.; Chen, X.; Wang, H.; Ji, S.; Huo, Y. The effects of 1-and 3-positions substitutions on the photophysical properties of perylene and its application in thiol fluorescent probes. *Tetrahedron* **2022**, *104*, 132565.

(95) Lin, Y.-C.; She, N.-Z.; Chen, C.-H.; Yabushita, A.; Lin, H.; Li, M.-H.; Chang, B.; Hsueh, T.-F.; Tsai, B.-S.; Chen, P.-T.; Yang, Y.; Wei, K.-H. Perylene diimide-fused dithiophenepyrroles with different end groups as acceptors for organic photovoltaics. *ACS Appl. Mater. Interfaces* **2022**, *14*, 37990−38003.

(96) Dalapati, R.; Nandi, S.; Van Hecke, K.; Biswas, S. Fluorescence modulation of an aggregation-induced emission active ligand via rigidification in a coordination polymer and its application in singlet oxygen sensing. *Cryst. Growth Des.* **2019**, *19*, 6388−6397.